NASA Technical Paper 3449

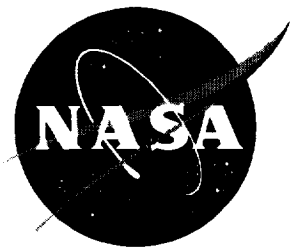

Optimal Control Theory Determination of Feasible Return-to-Launch-Site Aborts for the HL-20 Personnel Launch System Vehicle

Kevin E. Dutton
Langley Research Center • Hampton, Virginia

National Aeronautics and Space Administration
Langley Research Center • Hampton, Virginia 23681-0001

July 1994

Contents

Tables

Figures

Nomenclature

a	speed of sound, ft/sec
a_N, a_x	normal and axial load factors, respectively
a_0, a_1, a_2, a_3	coefficients for speed of sound polynomial
b	wingspan, ft
C_D	drag coefficient
$C_{D,0}, C_{D,1}, C_{D,2}$	coefficients for drag coefficient polynomial
C_L	lift coefficient
C_M	moment coefficient
$\mathbf{c}, \mathbf{d}$	state equality and inequality constraint vectors
D	drag force, lb
E	vehicle energy per unit mass, ft/sec^2
f	dynamical equations
$\mathbf{g}, \mathbf{h}$	control equality and inequality constraint vectors
g	magnitude of gravitational acceleration, ft/sec^2
g_0	magnitude of gravitational acceleration at sea level, ft/sec^2
h	altitude, ft
J	cost function
K	set of attainability
L	lift force, lb
l	vehicle length
M	Mach number
m	mass, slugs
$\mathbf{p}, \mathbf{q}$	hodograph equality and inequality constraint vectors
$\bar{q}$	dynamic pressure, $\frac{1}{2}\rho V^2$, lb/ft^2
R_E	radius of Earth, ft
r	distance of HL-20 cg from center of Earth, ft
S	hodograph
S_{ref}	HL-20 wing area, ft^2
t	time, sec
$\mathbf{u}$	control vector
V	velocity, ft/sec
W	empty weight, lb
W_{OMS}	OMS fuel weight, lb
$\mathbf{X}$	vector of unknowns in optimal control problem
$\mathbf{x}$	state vector

x	flat Earth east measurement, ft
x_{cg}	center of gravity location, percent body length
x_{ref}	moment reference center, percent body length
y	flat Earth north measurement, ft
α	angle of attack, deg
β	density scale height, ft^{-1}
γ	flight path angle, deg
Δ	aerodynamic coefficient increment due to control surface deflection
δ	control surface deflection, deg
θ	longitude, deg
λ	latitude, deg
ρ	density, $\mathrm{slugs/ft}^3$
ρ_0	sea level density, $\mathrm{slugs/ft}^3$
σ	bank angle, deg
ϕ	cost function
Ψ	boundary conditions
ψ	heading angle, deg
Ω	set of admissible controls

Subscripts:

e	wing flaps
f	final time
l	lower body flaps
T	total aerodynamic quantity
u	upper body flaps
V	basic vehicle (control surfaces undeflected)
0	initial time

Abbreviations:

cg	center of gravity
ATO	abort to orbit
CCAFS	Cape Canaveral Air Force Station
ELV	expendable launch vehicle
KSC	Kennedy Space Center
OMS	Orbital Maneuvering System
PLS	Personnel Launch System
RTLS	return to launch site
SRM	solid rocket motor
TAL	transatlantic abort landing

Abstract

The Personnel Launch System (PLS) being studied by NASA is a system to complement the Space Shuttle and provide alternative access to space. The PLS consists of a manned spacecraft launched by an expendable launch vehicle (ELV). A candidate for the manned spacecraft is the HL-20 lifting body. In the event of an ELV malfunction during the initial portion of the ascent trajectory, the HL-20 will separate from the rocket and perform an unpowered return-to-launch-site (RTLS) abort. This work details an investigation, using optimal control theory, of the RTLS abort scenario. The objective of the optimization was to maximize final altitude. With final altitude as the cost function, the feasibility of an RTLS abort at different times during the ascent was determined. The method of differential inclusions was used to determine the optimal state trajectories, and the optimal controls were then calculated from the optimal states and state rates.

1. Introduction

NASA is currently studying concepts for a new generation of manned space vehicles. This system is known as the Personnel Launch System (PLS). One design under consideration is a lifting body designated the HL-20 (fig. 1), which would be placed in orbit by an expendable launch vehicle (ELV) like the Titan III. The HL-20 is similar to previous lifting body vehicles that NASA has studied, such as the HL-10, the Martin Marietta X-24A, and the Northrop M2-F2 (ref. 1).

An HL-20 mission would begin with a vertical launch into low Earth orbit. It is assumed that the launch site would be the Kennedy Space Center (KSC) at Cape Canaveral, Florida. Once in orbit, the HL-20 will carry out such primary duties as a space station crew transfer or satellite repair. When returning to Earth, the vehicle will reenter the atmosphere and glide to a horizontal landing in a manner similar to the Space Shuttle orbiter.

1.1. Description of Abort Scenarios

One area of study for the HL-20 mission is that of aborts during the ascent phase. Five abort modes were investigated in references 2 and 3. These are (1) on the pad, (2) return to launch site (RTLS), (3) ocean landing by parachute, (4) transatlantic abort landing (TAL), and (5) abort to orbit (ATO). A description of these abort scenarios follows.

On-the-pad aborts would occur when a problem is detected with the booster while the HL-20 is mounted on top of the ELV at the launch pad. This would necessitate that the crew be removed a safe distance from the rocket in a short period of time. This abort would begin by firing a solid rocket motor (SRM) to remove the HL-20 from the ELV, and then the HL-20 would glide to the Cape Canaveral Air Force Station (CCAFS) skid strip or to the KSC Shuttle Landing Facility for a horizontal landing.

Immediately after launch and until 20 sec into the ascent phase, the vehicle could perform an RTLS abort to the Shuttle Landing Facility. Between 20 and 64 sec the vehicle could glide back to the CCAFS skid strip. The RTLS abort to the skid strip will be examined in detail in this paper. Figure 2 shows the locations of Pad 40, the skid strip, and the Shuttle Landing Facility at KSC.

Between 65 and 430 sec the abort option would be to parachute to an ocean landing. Beginning at 430 sec the vehicle could perform a TAL at one of the current Space Shuttle orbiter emergency landing sites. An ATO would be chosen from 490 to 510 sec.

1.2. Optimal Control Theory

The problem of determining the feasibility of an RTLS abort at some time during the Titan III/ HL-20 ascent phase is essentially that of an aerospace vehicle performing a minimum energy glide and turn through the atmosphere to a point above a runway, meeting some final boundary conditions, and satisfying some state and control equality and inequality constraints during the maneuver. Optimal control theory has been applied to the problem of hypersonic glide in reference 4. Chern and Vinh considered the problem of maximum downrange distance and other cost functions for both flat Earth and spherical Earth models. They investigated the optimal control problem by using the calculus of variations approach to

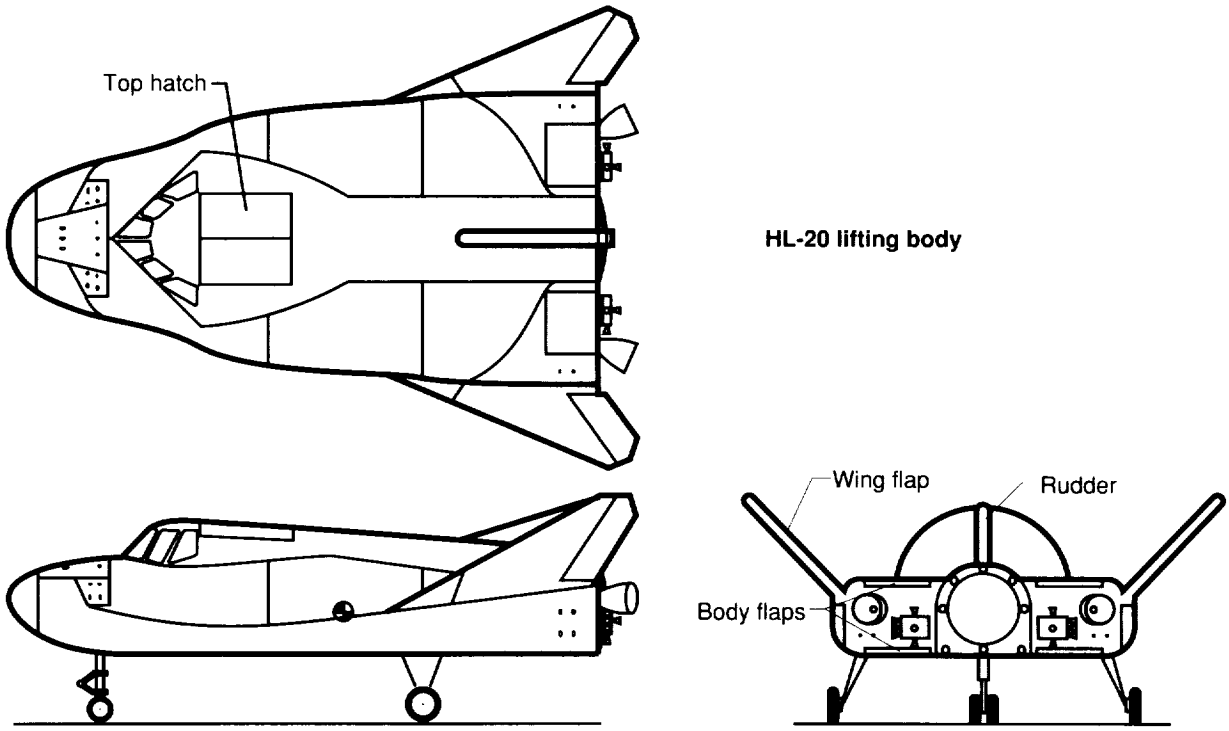

Figure 1. HL-20 lifting body.

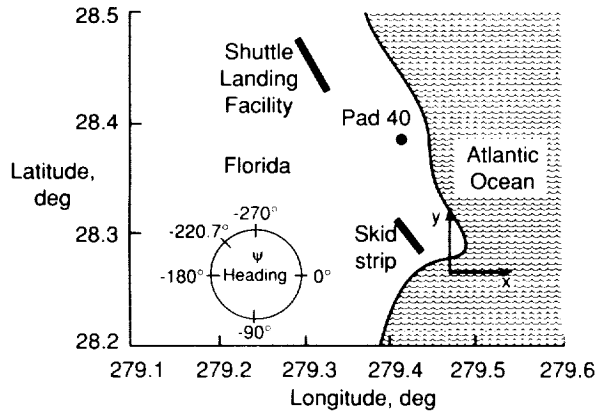

Figure 2. KSC runway and launch pad locations.

derive the first-order necessary conditions for optimality described in reference 5. For each problem considered, the assumption of constant Mach number was made in reference 4. Much of the work dealt with two-dimensional cases; the three-dimensional cases investigated were maximum cross-range distance and footprint calculation.

1.3. Purpose of Work

The use of optimal control theory applied to an RTLS problem could determine the ultimate RTLS performance of the HL-20, whereas the application of a simulation tool with less optimization capability may not. In the actual RTLS problem, the vehicle must be flown back to a point at which it can safely make the designated runway. To apply optimal control theory to the RTLS problem, however, careful thought must be given to the choice of a suitable cost function. In this work, final altitude was chosen as the cost function. A solution to this optimal control problem will determine the feasibility of an RTLS abort, but will not determine the actual RTLS trajectory to be flown (except in two cases the earliest and latest times at which an RTLS abort is possible).

In section 2 the HL-20 vehicle is described in detail and the aerodynamic, atmospheric, and dynamic models are presented. Section 3 introduces the concept of the hodograph, or state rate space. The solution method and its application to the HL-20 RTLS problem in two and three dimensions is discussed in this section. In section 4 results are presented for the feasible RTLS aborts along the ascent trajectory.

2. Vehicle and Model Description

2.1. Vehicle Description

A three-view drawing of the HL-20 vehicle is shown in figure 1, which depicts the seven control surfaces of the HL-20: rudder, two upper body flaps, two lower body flaps, and two wing flaps. The

surface deflection limits for the control surfaces are as follows: $\pm 30^\circ$ for the wing flaps, 0° to $+60^\circ$ for the lower body flaps, and -60° to 0° for the upper body flaps. A positive surface deflection is taken as trailing edge down for the wing and body flaps. In this investigation, the effect of the rudder was ignored.

Table I gives geometrical and physical parameters of the HL-20. The HL-20 is assumed to have an empty weight of 22 932 lb and 2948 lb fuel for the Orbital Maneuvering System (OMS) for a total weight of the HL-20 at liftoff of 25 880 lb. The center of gravity (cg) location for the empty vehicle is 55.5 percent of the vehicle length l (where 0 percent would represent the nose) and the cg location for the vehicle with full OMS fuel is 57.5 percent. It is assumed in this study that an abort would occur with a full load of OMS fuel.

Table I. HL-20 Physical Parameters

Vehicle length l, ft	27.31
Span b, ft	13.89
Wing area S_{ref}, ft^2	286.45
Empty weight W, lb	22 932
OMS fuel weight W_{OMS}, lb	2948
cg location (empty) x_{cg}, percent	55.5
cg location (full) x_{cg}, percent	57.5

2.2. Aerodynamics

The aerodynamic data for the HL-20 was taken from reference 6. Coefficients for cubic polynomial expressions for drag coefficient C_D, lift coefficient C_L, and moment coefficient C_M for the basic vehicle (control surfaces undeflected) are given as functions of angle of attack α, at various Mach numbers M. The aerodynamic coefficients were given for α ranging from -2° to 16° (and sometimes higher) and for M ranging from 0.3 to 4.0. Plots of C_D and C_L against α for several values of M are shown in figures 3 and 4. Reference 6 also provides coefficients for cubic polynomials for increments in C_D, C_L, and C_M due to the control surface deflections δ as a function of α for several values of δ and M.

It is important that the vehicle be flown within its trim envelope. Since the vehicle uses the body and wing flaps to accomplish this, it is probable that at some flight conditions a unique configuration of surface deflections to trim the vehicle would not exist. Therefore, in order to obtain trim C_D and trim C_L values as functions of α and M, a nonlinear parameter optimization problem was formulated that

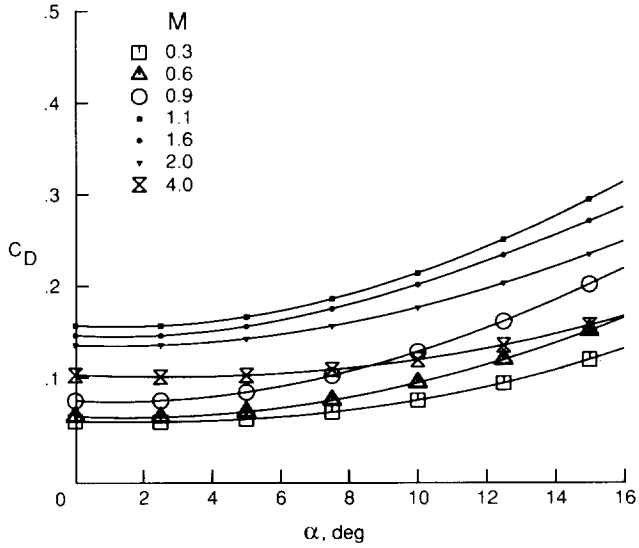

Figure 3. Basic HL-20 vehicle drag coefficient.

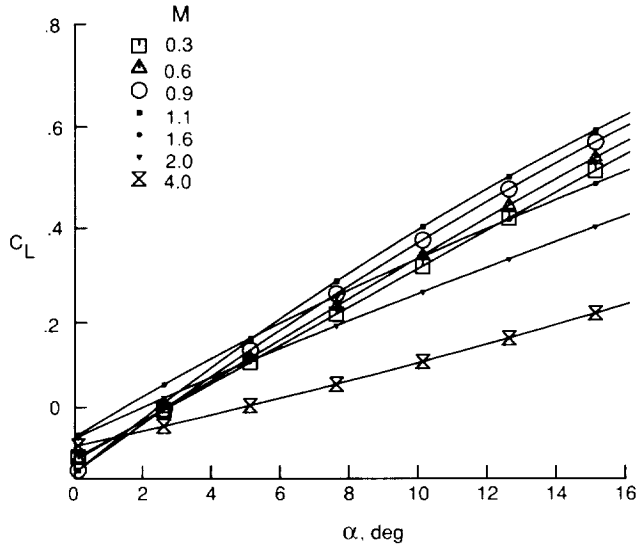

Figure 4. Basic HL-20 vehicle lift coefficient.

at every combination of α and M, would minimize the total drag coefficient $C_{D,T}$ of the vehicle while also trimming the vehicle. The independent variables that would accomplish this were the upper body flap deflection δ_u, lower body flap deflection δ_l, and the wing flap deflection δ_e.

The problem is to minimize the cost function

$$J = C_{D,T} = C_{D,V} + 2\Delta C_{D,u} + 2\Delta C_{D,l} + 2\Delta C_{D,e} \quad (2.1)$$

over the parameters δ_u, δ_l, and δ_e, where $C_{D,V}$ is the basic (control surfaces undeflected) vehicle drag, and $\Delta C_{D,u}$, $\Delta C_{D,l}$, and $\Delta C_{D,e}$ are the increments

to the total drag coefficient due to the deflections of the upper body flaps, lower body flaps, and wing flaps, respectively. Each incremental contribution is doubled, since increments to the coefficients are given for the right or left components of a control surface that is assumed to act symmetrically (left and right flaps deflect equally). The trim condition to be satisfied is

$$C_{M,T}+(C_{L,T}\cos\alpha + C_{D,T}\sin\alpha)(x_{cg} - x_{ref}) = 0 \quad (2.2)$$

where, in a similar fashion as $C_{D,T}$,

$$C_{L,T} = C_{L,V} + 2\Delta C_{L,u} + 2\Delta C_{L,l} + 2\Delta C_{L,e} \quad (2.3)$$

$$C_{M,T} = C_{M,V} + 2\Delta C_{M,u} + 2\Delta C_{M,l} + 2\Delta C_{M,e} \quad (2.4)$$

and x_{ref} is the location of the moment reference center from reference 6 and is equal to 54.0 percent. The center of gravity location x_{cg} for this problem was for full OMS fuel. (See table I.) The basic vehicle aerodynamic coefficients are functions of α and M, and the increments of the coefficients are functions of α, M, and surface deflection.

This nonlinear programming problem was solved at all values of α and M for which data is given from reference 6. The code NPSOL (ref. 7), a set of Fortran subroutines that minimize a function subject to linear and nonlinear constraints and bounds on the parameters, was used to solve the nonlinear programming problem. Solutions were obtained through the full range of α ($-2°$ to $16°$) at all Mach numbers except 1.6, 2.0, and 2.5. Table II summarizes the results of the above parameter optimization problem, presenting maximum trim α, and maximum and minimum trim C_L. The minimum trim C_L occurred for each Mach number at $\alpha = -2°$. Figure 5 plots the minimum and maximum trim C_L values against Mach number.

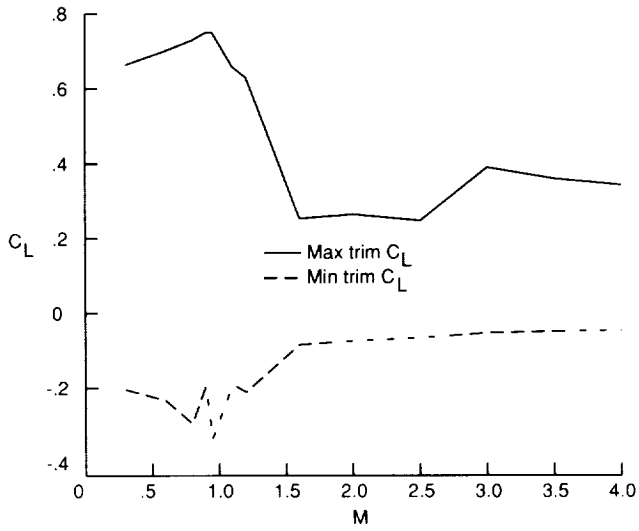

Figure 5. Minimum and maximum trim C_L.

Once values of trim C_D and C_L were determined for all possible values of α and M, a curve-fit of the form

$$C_D = C_{D,0}(M) + C_{D,1}(M)C_L + C_{D,2}(M)C_L^2 \quad (2.5)$$

was made at each value of M. The values of $C_{D,0}$, $C_{D,1}$, and $C_{D,2}$ are displayed in table III and plotted in figures 6, 7, and 8. To determine these coefficients at Mach numbers other than those in the table, a spline routine is used.

Table II. Maximum Trim α and C_L

M	α_{max}, deg	$C_{L,max}$	$C_{L,min}$
0.3	16.0	0.6628	−0.2045
.6	16.0	.7009	−.2340
.8	16.0	.7285	−.2949
.9	16.0	.7487	−.1950
.95	16.0	.7491	−.3357
1.1	16.0	.6574	−.1906
1.2	16.0	.6288	−.2106
1.6	9.4	.2537	−.0838
2.0	10.6	.2643	−.0737
2.5	12.0	.2477	−.0658
3.0	16.0	.3895	−.0530
3.5	16.0	.3592	−.0489
4.0	16.0	.3422	−.0457

Table III. Coefficients for C_D Expression

M	$C_{D,0}$	$C_{D,1}$	$C_{D,2}$
0.3	0.0438	−0.0200	0.3263
.6	.0473	−.0169	.3783
.8	.0491	−.0151	.4171
.9	.0788	−.1014	.5310
.95	.0756	−.0240	.4636
1.1	.1640	−.1605	.7288
1.2	.1534	−.0774	.6507
1.6	.1494	.0098	.8535
2.0	.1410	.0625	.3606
2.5	.1270	.0266	.6474
3.0	.1167	−.0499	.9923
3.5	.1101	−.0325	1.0738
4.0	.1080	−.0121	1.0992

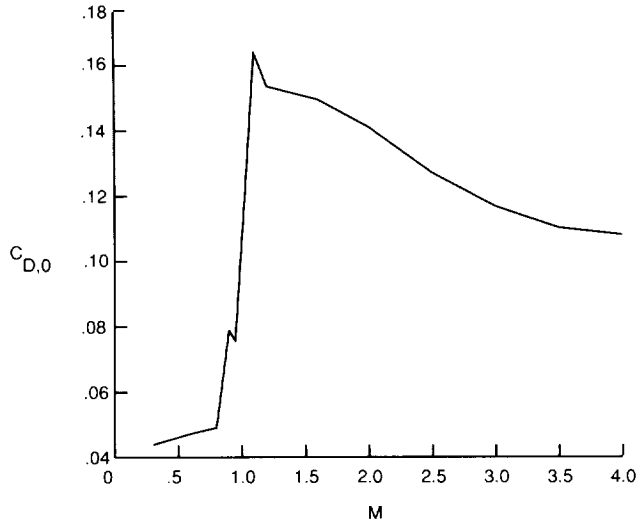

Figure 6. $C_{D,0}$ zeroth-order coefficient for C_D.

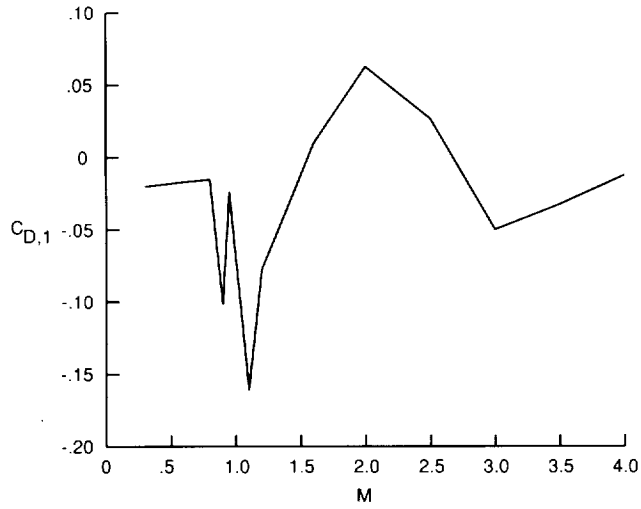

Figure 7. $C_{D,1}$ first-order coefficient for C_D.

2.3. Atmospheric and Gravitational Model

With the 1962 U.S. Standard Atmosphere (ref. 8) as a reference, an exponential curve-fit was made to density ρ in the altitude range h from sea level to 150 000 ft. The sea level density value ρ_0 of the exponential model matched the standard atmosphere model. The model is given by

$$\rho = \rho_0 e^{-\beta h} \tag{2.6}$$

A cubic polynomial was fit to the standard atmosphere variation of speed of sound a with altitude. This model is of the form

$$a = a_0 + a_1 h + a_2 h^2 + a_3 h^3 \tag{2.7}$$

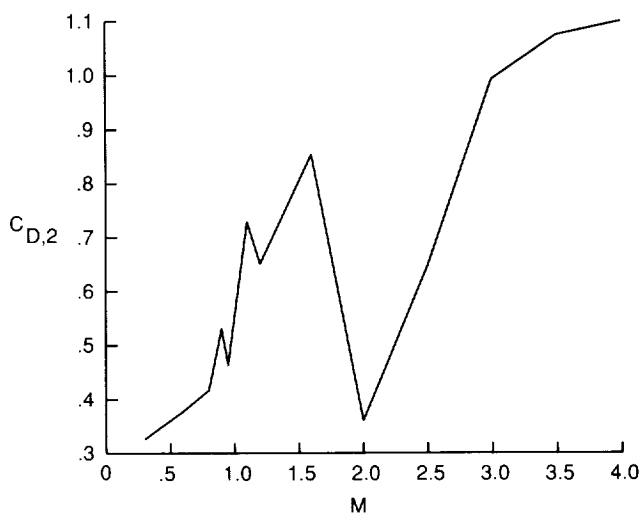

Figure 8. $C_{D,2}$ second-order coefficient for C_D.

An inverse square gravitational model was used of the form

$$g = g_0 \left(\frac{R_E}{R_E + h} \right)^2 \tag{2.8}$$

where R_E is the radius of the Earth and g_0 is the sea level gravity. The coefficients and parameters for equations (2.6), (2.7), and (2.8) are given in table IV.

Table IV. Parameters for Atmospheric and Gravitational Models

ρ_0, slug/ft^3	2.3769×10^{-3}
β, ft^{-1}	3.6000×10^{-5}
a_0, ft/sec	1.1235×10^{3}
a_1, sec^{-1}	-5.7923×10^{-3}
a_2, ft^{-1}-sec^{-1}	6.2641×10^{-8}
a_3, ft^{-2}-sec^{-1}	-1.7708×10^{-13}
g_0, ft/sec^2	3.2174×10^{1}
R_E, ft	2.0926×10^{7}

2.4. Dynamic Model

The equations of motion for a point mass, nonthrusting aerospace vehicle over a spherical, nonrotating planet may be defined with six states. These states are altitude h, longitude θ, latitude λ, velocity V, flight path angle γ, and heading ψ. The governing equations of motion are (ref. 4)

$$\dot{h} = V \sin\gamma \tag{2.9}$$

$$\dot{\theta} = \frac{V \cos\gamma \cos\psi}{r \cos\lambda} \tag{2.10}$$

$$\dot{\lambda} = \frac{V \cos\gamma \sin\psi}{r} \tag{2.11}$$

$$\dot{V} = -\frac{D}{m} - g\sin\gamma \tag{2.12}$$

$$\dot{\gamma} = \frac{L}{mV}\cos\sigma - \left(\frac{g}{V} - \frac{V}{r}\right)\cos\gamma \tag{2.13}$$

$$\dot{\psi} = \frac{L}{mV\cos\gamma}\sin\sigma - \frac{V}{r}\cos\gamma\cos\psi\tan\lambda \tag{2.14}$$

where $r = R_E + h$, m is the vehicle mass, D is the drag force, L is the lift force, and σ is the bank angle. The heading angle is zero for due east flight and increases in a counterclockwise direction. Figure 2 shows a heading cylinder with different values of ψ corresponding to different flight directions. From the back of the vehicle, the bank angle σ is zero when the lift vector points directly upward, and increases as the lift vector rotates counterclockwise from the vertical. The lift and drag forces are given by

$$L = \frac{1}{2}\rho S_{\text{ref}} V^2 C_L \tag{2.15}$$

$$D = \frac{1}{2}\rho S_{\text{ref}} V^2 C_D \tag{2.16}$$

where S_{ref} is the total wing area of the HL-20.

In the time between the launch and the commencement of an RTLS abort, the vehicle distance from the landing strip is small compared with the radius of the Earth. Also, the maximum speed the vehicle attains during an RTLS abort is much smaller than orbital velocity. These two conditions lead to the use of the simpler flat Earth equations of motion:

$$\dot{h} = V\sin\gamma \tag{2.17}$$

$$\dot{x} = V\cos\gamma\cos\psi \tag{2.18}$$

$$\dot{y} = V\cos\gamma\sin\psi \tag{2.19}$$

$$\dot{V} = -\frac{D}{m} - g\sin\gamma \tag{2.20}$$

$$\dot{\gamma} = \frac{L}{mV}\cos\sigma - \frac{g}{V}\cos\gamma \tag{2.21}$$

$$\dot{\psi} = \frac{L}{mV\cos\gamma}\sin\sigma \tag{2.22}$$

In this system, longitude and latitude have been replaced with flat Earth Cartesian coordinates x and y. The origin of the x-y system is a point on the extended skid strip centerline, 10 725 ft southeast of the skid strip threshold. The x-axis points east and the y-axis north. The location and orientation of this coordinate system is shown in figure 2.

The controls for this problem are the lift coefficient C_L and the bank angle σ, which together specify the magnitude and direction of the aerodynamic lift vector.

3. Hodograph Analysis and Solution Method

In this section optimal control theory and the concept of the hodograph are discussed. The hodograph leads directly to the concept of the set of attainability and to the method of differential inclusions, which is used to solve the optimal control problems presented in this work. A two-dimensional maximum final altitude problem is presented, and the solution method as applied to this problem is discussed. This discussion is then extended to a problem in three dimensions representing the HL-20 RTLS abort problem.

3.1. Optimal Control Theory

A general optimal control problem involves finding the control function $\mathbf{u}(t)$ that maximizes a scalar cost function

$$J = \phi[\mathbf{x}(t_f)] \tag{3.1}$$

subject to the differential constraints

$$\dot{\mathbf{x}}(t) = \mathbf{f}[\mathbf{x}(t), \mathbf{u}(t)] \quad (t_0 \le t \le t_f) \tag{3.2}$$

where $\mathbf{x} \in \mathbf{R}^n$ is the state vector, $\mathbf{u} \in \mathbf{R}^m$ is the control vector, and t is the time. Assume free final time t_f for this problem. Some of the states at the initial and final times, t_0 and t_f, may be given in the form

$$\Psi[\mathbf{x}(t_0), \mathbf{x}(t_f)] = 0 \tag{3.3}$$

In addition, there may be control and state equality and inequality constraints of the form

$$\mathbf{g}[\mathbf{x}(t), \mathbf{u}(t)] = 0 \tag{3.4}$$

$$\mathbf{h}[\mathbf{x}(t), \mathbf{u}(t)] \le 0 \tag{3.5}$$

$$\mathbf{c}[\mathbf{x}(t)] = 0 \tag{3.6}$$

$$\mathbf{d}[\mathbf{x}(t)] \le 0 \tag{3.7}$$

Equations (3.1) (3.7) constitute an optimal control problem. For a derivation of the necessary conditions that must be satisfied for $\mathbf{u}(t)$ to be a solution of the above problem, see reference 5.

3.2. The Hodograph and the Set of Attainability

The notation of reference 9 is adopted to discuss the hodograph. For a set of states $\mathbf{x}$, the hodograph, or state-rate space, is defined as the set of all possible

state rates $\dot{\mathbf{x}}$ that can be achieved by varying the controls within their permissible limits. The hodograph can be represented by

$$S(\mathbf{x}) = \{\dot{\mathbf{x}} \in \mathbf{R}^n | \dot{\mathbf{x}} = f(\mathbf{x}, \mathbf{u}), \mathbf{u} \in \Omega(\mathbf{x})\} \quad (3.8)$$

where $\Omega(\mathbf{x})$ is the set of admissible controls:

$$\Omega(\mathbf{x}) = \{\mathbf{u} \in \mathbf{R}^m | \mathbf{g}(\mathbf{x}, \mathbf{u}) = 0, \mathbf{h}(\mathbf{x}, \mathbf{u}) \leq 0\} \quad (3.9)$$

The controls can then be thought of as an instrument for parameterizing the hodograph. The optimal state history and optimal cost associated with the optimal control problem defined in equations (3.1) (3.7) will be unchanged if the control vector is replaced by any other set of variables (with the appropriate control constraint functions, eqs. (3.4) and (3.5)), so long as the hodograph remains unchanged.

As described in reference 9, it is assumed that the controls can be expressed in terms of the states and state rates so that there are smooth functions $\mathbf{p}$ and $\mathbf{q}$ such that the hodograph can be rewritten as

$$S(\mathbf{x}) = \{\dot{\mathbf{x}} \in \mathbf{R}^n | \mathbf{p}(\dot{\mathbf{x}}, \mathbf{x}) = 0, \mathbf{q}(\dot{\mathbf{x}}, \mathbf{x}) \leq 0\} \quad (3.10)$$

The information from equations (3.8) and (3.9) has been combined into equation (3.10) and the hodograph has been expressed entirely in terms of states and state rates, with no controls present. The presence of the inequality constraints $\mathbf{q}$ in equation (3.10) implies that the state rates can take on values within the range of permissible state rates as determined by the admissible controls. Therefore, instead of specifying the value of the state rates as in a differential equation, we choose the state rates from among their permissible values. This is the concept of differential inclusions.

Now define the set of attainability $K(t_0, \mathbf{x}_0; t_1)$ as the set of all states to which the state vector $\mathbf{x}_0$ at t_0 can be steered to at time t_1 by varying the controls through the admissible range. The set of attainability has a direct relationship to the hodograph and, for a small enough time step, can be approximated to first order by using the hodograph. Let Δt be the small time step and let $t_1 = t_0 + \Delta t$. Approximate the set of attainability by

$$\tilde{K}(t_0, \mathbf{x}_0; t_1) = \{\mathbf{x} \in \mathbf{R}^n | \mathbf{x} = \mathbf{x}_0 + \Delta t \cdot S(\mathbf{x}_0)\} \quad (3.11)$$

When Δt is small enough, it can be seen that the states at neighboring times are related by the hodograph and the set of attainability concepts. In an optimal control problem, the states must be chosen to maximize the cost function J, and neighboring states must lie within the set of attainability as determined by the state rates and the time step. The range of state rate values is determined by the admissible controls. If a first-order approximation to the state rates is made using the values of the states at two nodal points, the problem has been reduced to a determination of the optimal states only, with constraints specifying the set of attainability.

3.3. Numerical Approach

Subdivide the time interval, which, without loss of generality, is assumed to be $t \in [0, 1]$ into N equal subintervals. Then the $N + 1$ nodes can be represented by

$$t_i = \frac{i}{N} \quad (3.12)$$

where $i = 0, 1, 2, ..., N$. Let the vector $\mathbf{X}$ be of length $n \cdot (N + 1)$ representing the state vector $\mathbf{x}$ at the nodes, where $\mathbf{x} \in \mathbf{R}^n$. The optimization problem is now to find the vector $\mathbf{X}$ that will minimize the cost function

$$J = \phi[\mathbf{x}(t_N)] \quad (3.13)$$

subject to the boundary conditions

$$\Psi[\mathbf{x}(t_0), \mathbf{x}(t_N)] = 0 \quad (3.14)$$

If the state rates are approximated by

$$\dot{\bar{\mathbf{x}}}_i = \frac{\mathbf{x}_{i+1} - \mathbf{x}_i}{\Delta t} \quad (3.15)$$

and the states by

$$\bar{\mathbf{x}}_i = \frac{\mathbf{x}_i + \mathbf{x}_{i+1}}{2} \quad (3.16)$$

then the necessary constraints are

$$\left.\begin{aligned} \mathbf{p}(\dot{\bar{\mathbf{x}}}_i, \bar{\mathbf{x}}_i) &= 0 \\ \mathbf{q}(\dot{\bar{\mathbf{x}}}_i, \bar{\mathbf{x}}_i) &\leq 0 \end{aligned}\right\} \quad (3.17)$$

where $i = 0, 1, 2, ..., N - 1$. In equations (3.15) (3.17), the simple Euler approximation in equation (3.11) has been replaced by a more precise midpoint rule.

The problem has become one of finding the states at the nodes that optimize the cost function subject to the boundary conditions and the equality and inequality constraints $\mathbf{p}$ and $\mathbf{q}$. These two constraint vectors contain the dynamical information and must be satisfied at the midpoint of each node. In other words, a nonlinear programming problem must be solved, where the parameters are the states at the nodes. The code NPSOL was used to solve the nonlinear programming problem.

3.4. HL-20 RTLS Abort—Hodograph Analysis

The use of this solution method for the HL-20 RTLS abort problem defined in the previous section is now examined. For a solution of the optimal control problem to exist, it is required that the hodograph be convex and that the optimal state rates be on the boundary of or within the hodograph. This implies using inequality constraints to specify the surface and interior of the hodograph. To explain how this is done, the hodograph of a two-dimensional nonthrusting aerospace vehicle over a flat Earth is examined. With this as a foundation, the concepts are then extended to the full three-dimensional problem.

3.4.1. Two-dimensional case. The optimal RTLS abort problem in two or three dimensions is to maximize the cost function

$$J = h(t_f) \tag{3.18}$$

or, equivalently, to minimize the cost function

$$J = -h(t_f) \tag{3.19}$$

The equations of motion for the two-dimensional case are

$$\dot{h} = V \sin\gamma \tag{3.20}$$

$$\dot{x} = V \cos\gamma \tag{3.21}$$

$$\dot{V} = -\frac{\rho V^2 S C_D}{2m} - g \sin\gamma \tag{3.22}$$

$$\dot{\gamma} = \frac{\rho V S C_L}{2m} - \frac{g}{V}\cos\gamma \tag{3.23}$$

where h, x, V, and γ are defined as in section 2. The one control in this case is C_L, and C_D is again given by

$$C_D = C_{D,0} + C_{D,1}C_L + C_{D,2}C_L^2 \tag{3.24}$$

It is assumed that C_L is bounded by

$$0 \le C_L \le C_{L,\max} \tag{3.25}$$

Now select permissible values of the four states and determine the state rates from equations (3.20)–(3.23) as the control C_L varies throughout its admissible region given by equation (3.25). The result is a two-dimensional hodograph. Since the equations for $\dot{h}$ and $\dot{x}$ are independent of the control, the hodograph in the $\dot{h}, \dot{x}$ space is a single point whose coordinates are given by equations (3.20) and (3.21).

Figure 9 shows a drag polar as given by equation (3.24). If C_D and C_L from (3.22) and (3.23) are determined as

$$C_D = -\frac{2m}{\rho V^2 S}\left(\dot{V} + g\sin\gamma\right) \tag{3.26}$$

and

$$C_L = \frac{2m}{\rho V S}\left(\dot{\gamma} + \frac{g}{V}\cos\gamma\right) \tag{3.27}$$

then it is seen that the hodograph in the $\dot{V}, \dot{\gamma}$ space is similar to the drag polar in the C_L, C_D space but it is scaled and shifted. Equation (3.24) is the boundary of the two-dimensional hodograph.

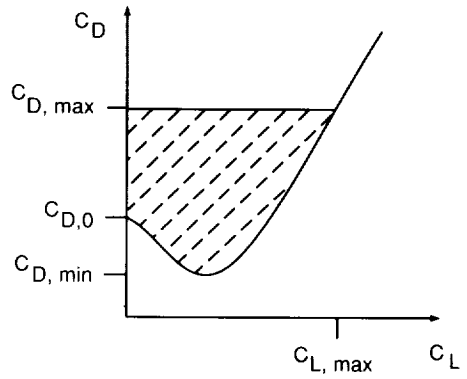

Figure 9. Drag polar (two-dimensional hodograph).

As stated previously, the optimal state rates must lie on the surface of, or within, this hodograph or drag polar. This requires that for some value of C_L, the value of C_D, given by equation (3.26), must be greater than or equal to the value of C_D on the drag polar, given by equation (3.24), or

$$-\frac{2m}{\rho V^2 S}\left(\dot{V} + g\sin\gamma\right) \ge C_{D,0} + C_{D,1}C_L + C_{D,2}C_L^2 \tag{3.28}$$

where C_L is given by equation (3.27). Since C_L is bounded, this implies an upper limit to C_D. Adding a constraint on the upper limit of C_D implies that it is necessary to search for the optimal state rates in the shaded region of figure 9. To do this, the constraint

$$-\frac{2m}{\rho V^2 S}\left(\dot{V} + g\sin\gamma\right) \le C_{D,\max} \tag{3.29}$$

where $C_{D,\max}$ is given by

$$C_{D,\max} = C_{D,0} + C_{D,1}C_{L,\max} + C_{D,2}C_{L,\max}^2 \tag{3.30}$$

is needed. Although the physics of this aerospace problem suggests that equation (3.28) should actually be an equality, the convexity condition of the

hodograph tells us that an inequality constraint is equivalent.

The parameter optimization problem must therefore satisfy the equality constraints

$$\dot{h} - V \sin\gamma = 0 \tag{3.31}$$

$$\dot{x} - V \cos\gamma = 0 \tag{3.32}$$

and the inequality constraints of equations (3.28) and (3.29). After the optimal states have been found from the nonlinear programming problem, the control C_L can be found from equation (3.27). For the two-dimensional case, the size of the equality constraint vector $\mathbf{p}$ is 2 (eqs. (3.31) and (3.32)), and the size of the inequality constraint vector $\mathbf{q}$ is 2 (eqs. (3.28) and (3.29)).

3.4.2. Three-dimensional case. Now this analysis is extended to the three-dimensional case. The cost function for this case will remain the same as for the two-dimensional case. In a similar fashion to equations (3.31) and (3.32), the differential equations for altitude, downrange distance, and crossrange distance (h, x, and y) lead to the three equality constraints that must be satisfied

$$\dot{h} - V \sin\gamma = 0 \tag{3.33}$$

$$\dot{x} - V \cos\gamma \cos\psi = 0 \tag{3.34}$$

$$\dot{y} - V \cos\gamma \sin\psi = 0 \tag{3.35}$$

To determine the necessary hodograph inequality constraints, the two-dimensional hodograph is rotated about the vertical, or C_D, axis. This three-dimensional hodograph is shown in figure 10. The rotated drag polar in the $C_L \cos\sigma$, $C_L \sin\sigma$, and C_D space is similar to the hodograph in the $\dot{V}$, $\dot{\gamma}$, and $\dot{\psi}$ space, since

$$C_L \sin\sigma = \frac{2m}{\rho V S}\left(\dot{\psi}\cos\gamma\right) \tag{3.36}$$

$$C_L \cos\sigma = \frac{2m}{\rho V S}\left(\dot{\gamma} + \frac{g}{V}\cos\gamma\right) \tag{3.37}$$

$$C_D = -\frac{2m}{\rho V^2 S}\left(\dot{V} + g\sin\gamma\right) \tag{3.38}$$

Once again, the hodograph in the $\dot{V}$, $\dot{\gamma}$, and $\dot{\psi}$ space is a scaled and translated version of the rotated drag polar in the $C_L \cos\sigma$, $C_L \sin\sigma$, and C_D space.

Note that since the two-dimensional drag polar is not symmetric about the C_D axis (because of the linear $C_{D,1}$ term) the rotated three-dimensional drag polar is not convex. It can be seen that the minimum value of $C_D(C_{D,\min})$ is less than $C_{D,0}$, and so the bottom of the three-dimensional hodograph appears to be pushed upward into the interior of the convex hull of the hodograph. The three-dimensional hodograph could be made convex by requiring that when C_L is less than the value of C_L for $C_{D,\min}(C_L|_{C_{D,\min}})$ then

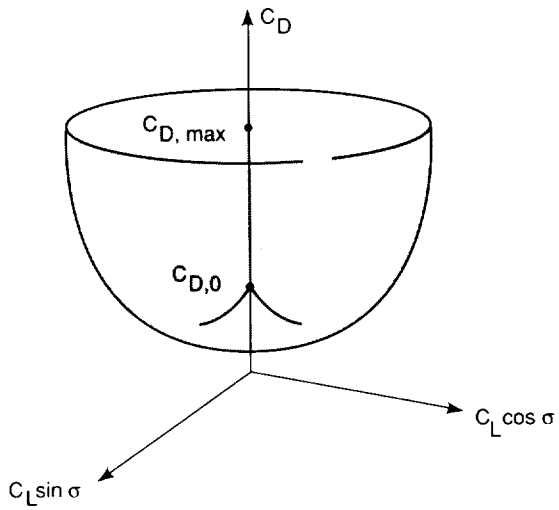

Figure 10. Rotated drag polar (three-dimensional hodograph).

$$C_D = C_{D,\min} \tag{3.39}$$

This flattens out the hodograph at the bottom and is known as relaxing the problem. For a discussion of the convex hull of the hodograph and relaxing an optimal control problem, see reference 10. It was found that it was not necessary to relax the problem because the optimal values of C_L, as determined from the optimal states and state rates, showed that C_L is always larger than $C_L|_{C_{D,\min}}$.

To calculate the controls for the three-dimensional case, it is seen from equations (3.36) and (3.37) that the bank angle σ can be expressed as

$$\tan\sigma = \frac{\dot{\psi}\cos\gamma}{\dot{\gamma} + (g/V)\cos\gamma} \tag{3.40}$$

and the lift coefficient can be expressed as

$$C_L = \frac{2m}{\rho V S}\sqrt{\left(\dot{\psi}\cos\gamma\right)^2 + \left(\dot{\gamma} + \frac{g}{V}\cos\gamma\right)^2} \tag{3.41}$$

Equation (3.41) is similar to equation (3.27) but with a term to reflect the heading rate.

To restrict our search for the optimal state rates to the boundary or interior of the rotated drag polar,

Table V. Trajectory Conditions and Abort Initial Conditions at 30 Sec

	Trajectory conditions	Abort initial conditions
Altitude, ft	1.07025576×10^4	2.77408551×10^4
Velocity, ft/sec	8.04746952×10^2	1.01506581×10^3
Latitude, deg	2.84006296×10^1	2.84001727×10^1
Longitude, deg	2.79428431×10^2	2.79445672×10^2
Flight path angle, deg	7.11376932×10^1	6.49159663×10^1
Azimuth, deg	9.16395039×10^1	9.19469374×10^1

the same two inequality constraints as in the two-dimensional problem are needed, equations (3.28) and (3.29). The lift coefficient C_L is now given by equation (3.41) and not equation (3.27). So for the three-dimensional case, the size of the equality constraint vector $\mathbf{p}$ is 3 (eqs. (3.33) (3.35)), and the size of the inequality constraint vector $\mathbf{q}$ is again 2.

For each abort case considered, NPSOL was used to solve the nonlinear programming problem with 41 nodes. This resulted in a problem with 247 $(6 \times 41 + 1)$ independent variables representing the states at each node and the final time, 212 $(5 \times 40 + 12)$ constraints representing the 5 hodograph constraints that must be satisfied at the midpoint of each interval, 6 initial state boundary conditions, 5 final state boundary conditions, and a parameter representing the free final time. The number of hodograph constraints will be explained in the next section. The difference in the state histories between converged cases with 41 nodes and 101 nodes was examined and found to be insignificant; so in the interest of computational time, 41 nodes were used in all cases.

4. Results

In this section, the launch profile of the HL-20 vehicle boosted by a Titan III launch vehicle is first discussed. Then the mechanism for ELV/HL-20 separation is briefly described. Initial and final conditions for an RTLS abort are given, and results for RTLS aborts at three times along the ascent trajectory are presented.

4.1. Ascent Launch Profile

Throughout the investigation it is assumed that the HL-20 is delivered to orbit by a Titan III rocket. The ascent trajectory of this Titan III/HL-20 combination is given in reference 3. This ascent trajectory was determined from abort considerations for all portions of the trajectory. Only that portion of the ascent trajectory during which the HL-20 can safely return to the launch site is of interest in this investigation.

4.2. Separation Mechanism

Reference 3 describes the mechanism for separating the HL-20 from the Titan III. There are two sets of four SRM's to perform the separation. For RTLS aborts, four primary abort SRM's burn for 3.5 sec with a combined thrust of 248 800 lb. This is followed by four sustainer abort SRM's of 33 000 lb combined thrust burning for 12.5 sec. These solid rocket motors are required to get the HL-20 away from an exploding ELV. It is assumed that the OMS engines do not fire during the separation or during the RTLS abort glide back to the runway.

When an abort at time $t = T$ sec is discussed, it is understood that the initial abort conditions are the conditions at time T along the ascent trajectory, followed by the primary SRM's burn, followed by the sustainer SRM's burn (when possible). The initial conditions for an abort at time T along the ascent trajectory will then be the conditions at time T, followed by the 3.5-sec burn of the primary SRM, followed by the 12.5-sec sustainer SRM burn. The primary and sustainer SRM burns are assumed to occur for all abort cases except when noted otherwise.

4.3. Initial and Final Boundary Conditions

To understand the effect of the SRM burns on the HL-20 position and velocity, two flight conditions for the vehicle are presented in table V. The second column shows the conditions at $T = 30$ sec along the launch trajectory. The third column shows the conditions that would result if an RTLS abort commenced at $T = 30$ sec after launch (when the vehicle had the conditions given in the second column) with the two SRM burns. The SRM's have the primary effect of increasing the vehicle altitude and velocity. The position and heading do not change significantly during the firing of the SRM's for this case. As the ascent trajectory flattens out, however, the position is increasingly affected by the SRM burns.

The initial conditions for aborts beginning at times from 15 to 65 sec along the launch trajectory

Table VI. RTLS Abort Initial State Boundary Conditions

Time, sec	h, ft	x, ft	y, ft	V, ft/sec	γ, deg	ψ, deg
15.0	1.8745648×10^4	-5.7470680×10^3	4.5283500×10^4	1.0011717×10^3	5.2205378×10^1	-1.9757279×10^0
20.0	1.9542422×10^4	-1.4644223×10^4	4.5599964×10^4	9.2742651×10^2	7.8466266×10^1	-1.8261807×10^2
25.0	2.3134577×10^4	-9.1229215×10^3	4.5412128×10^4	9.6635809×10^2	6.9053372×10^1	-1.9055671×10^0
30.0	2.7740855×10^4	-6.3246933×10^3	4.5323737×10^4	1.0150658×10^3	6.4915966×10^1	-1.9469374×10^0
35.0	3.3599490×10^4	-3.2577126×10^3	4.5222760×10^4	1.1221480×10^3	6.5218080×10^1	-1.9956142×10^0
40.0	4.0475148×10^4	6.3478304×10^2	4.5090776×10^4	1.3057310×10^3	6.5236462×10^1	-2.0383687×10^0
45.0	4.7865123×10^4	6.0726763×10^3	4.4902247×10^4	1.5278721×10^3	6.2192217×10^1	-2.0711914×10^0
50.0	5.5686139×10^4	1.2990810×10^4	4.4656591×10^4	1.7782816×10^3	5.7285346×10^1	-2.1044202×10^0
55.0	6.4005911×10^4	2.1276190×10^4	4.4355667×10^4	2.0602513×10^3	5.2767337×10^1	-2.1401928×10^0
60.0	5.0263039×10^4	1.2722135×10^4	4.4203290×10^4	2.5275142×10^3	5.3469427×10^1	-3.0684166×10^0
65.0	5.8047153×10^4	2.0051551×10^4	4.4405061×10^4	2.7780916×10^3	5.0050729×10^1	-2.0997439×10^0

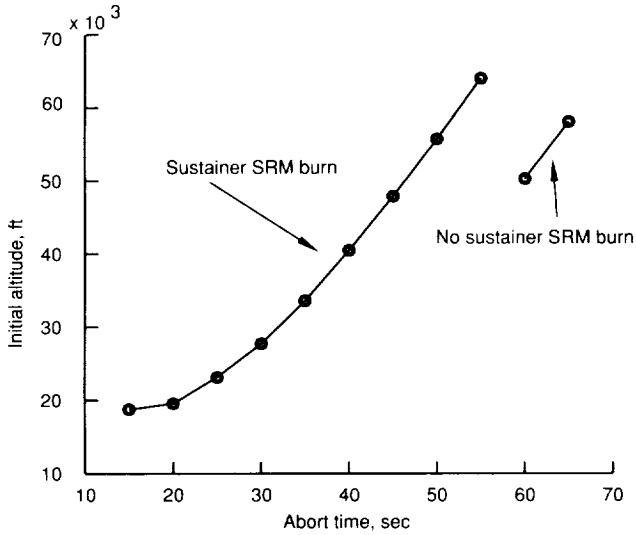

Figure 11. Initial altitude for HL-20 RTLS abort.

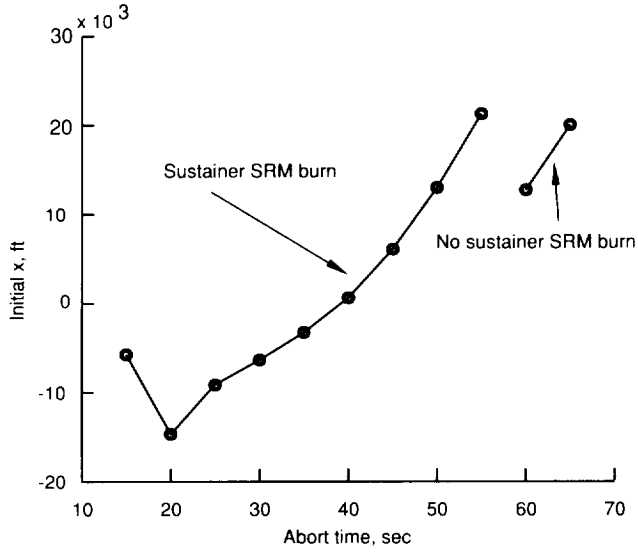

Figure 12. Initial x for HL-20 RTLS abort.

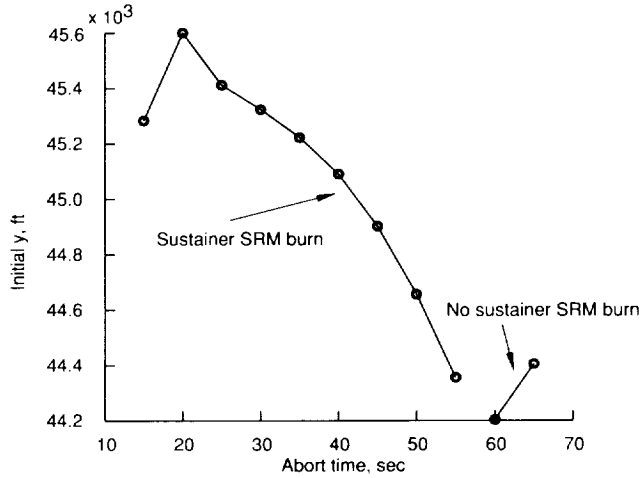

Figure 13. Initial y for HL-20 RTLS abort.

are given in table VI and also in figures 11–16. The sustainer SRM's burn is not used for the 60- and 65-sec cases because if they are fired, the vehicle is unable to return to the skid strip.

The final states are chosen as follows. In reference 3 a final altitude of 2000 ft and dynamic pressure of 300 lb/ft^2 were targeted, where dynamic pressure $\bar{q}$ is given by $\bar{q} = \frac{1}{2}\rho V^2$. These values correspond to a final velocity of 520.8 ft/sec. Although a different final altitude will result from a solution of the optimal control problem as posed, the same final velocity was targeted. As in reference 3, a final γ of $-19°$ was used.

The final location above the ground corresponded to a point on the extended centerline of the skid strip runway 31, displaced 10 725 ft to the southeast of the runway threshold. Since this point does not change for any of the cases examined, the origin of the x-y system was placed here so that $x(t_f) = y(t_f) = 0$.

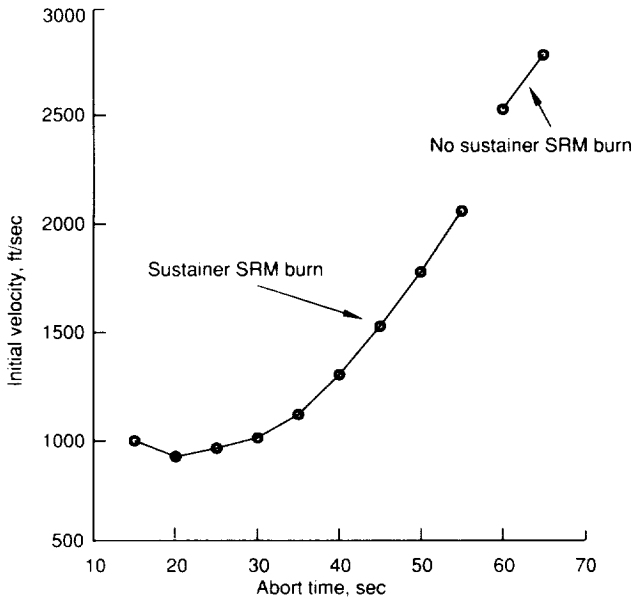

Figure 14. Initial velocity for HL-20 RTLS abort.

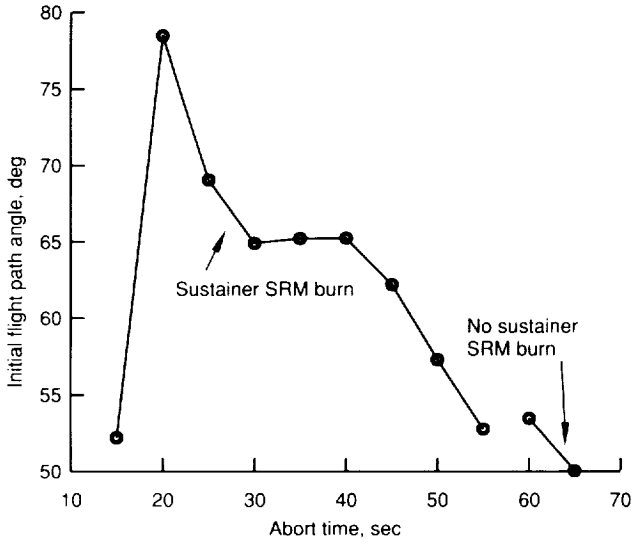

Figure 15. Initial flight path angle for HL-20 RTLS abort.

In latitude and longitude coordinates, this point is $\lambda(t_f) = 28°16'33''$ and $\theta(t_f) = 279°27'55''$. At this final point the vehicle should be lined up with the runway so it should have a final heading angle of $\psi(t_f) = -220.7°$. These final conditions are summarized in table VII.

A solution to the optimal control problem as posed will result in a trajectory that, in most cases, ends at an altitude well above the skid strip. It is assumed that some control logic exists that can steer the vehicle to any altitude lower than the maximum final altitude, while also meeting the terminal

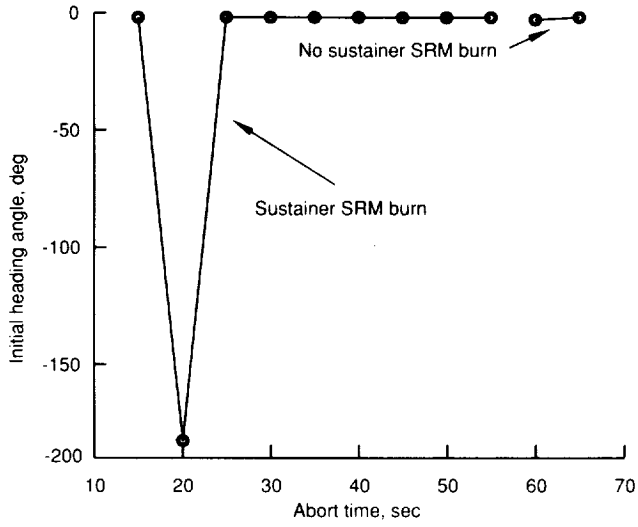

Figure 16. Initial heading angle for HL-20 RTLS abort.

Table VII. RTLS Abort Final State Boundary Conditions

x, ft	0.0
y, ft	0.0
V, ft/sec	520.8
γ, deg	−19.0
ψ, deg	−220.7

boundary conditions. Therefore, using final altitude as a cost function will determine the feasibility of an RTLS abort and will not determine the actual trajectory that should be flown back to the runway (except in two cases—the times of earliest and latest aborts, when the vehicle will be above the final point with only enough altitude to reach the skid strip and flare).

4.4. Results of RTLS Aborts

There will be some final critical altitude at the final (x, y) location below which the vehicle cannot glide back to the runway. The final altitude that was targeted in reference 3, $h(t_f) = 2000$ ft, will be used for this critical altitude. If the final optimal altitude is greater than this, under the assumption from the previous section, it is assumed that a successful landing following an RTLS abort is possible.

It was found that the vehicle could make it back to the skid strip between 15 sec and 65 sec into the launch. No data was available for the time before 15 sec. At 70 sec, the vehicle is too far from the skid strip to return and would have to land in the ocean by deploying a parachute.

The cost function (final altitude) is shown in figure 17 plotted against the time along the launch trajectory at which an abort procedure is initiated. It is seen that the final altitude in all cases is greater than the critical altitude of 2000 ft, which suggests that in all cases an abort is possible.

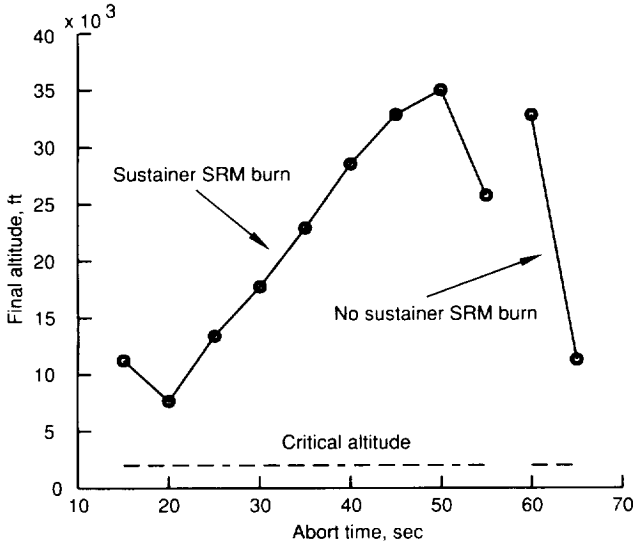

Figure 17. Cost function versus abort time.

The 15-, 30-, and 65-sec cases are now examined in detail. Figures 18 29 show the states and controls for RTLS aborts at these times. When states for an RTLS problem are plotted against time, $t = 0$ refers to the moment when the final SRM's (primary or sustainer) have ceased firing.

Figure 18 shows that the final altitudes were 11 200 ft, 17 700 ft, and 11 300 ft for the 15-, 30-, and 65-sec abort cases, respectively. Making the assumption that a control logic exists to steer the vehicle to 2000 ft if the final optimal altitude is greater than this, it is seen that in each case there is some altitude margin at the final point, and an RTLS abort is possible at 15, 30, and 65 sec into the launch.

Each abort case exhibits the same characteristic of trading velocity for altitude to reach some maximum altitude, and then continually losing altitude for the rest of the trajectory (fig. 18). It can be seen that the initial altitude increases as the launch time increases from 15 to 30 to 65 sec as the ELV/HL-20 climbs on its ascent trajectory. The 65-sec case is seen to have a much longer time of flight than the other two cases (280 sec compared to 120 sec).

The ground track of the three cases shows the eastward travel of the ELV as it ascends from 15

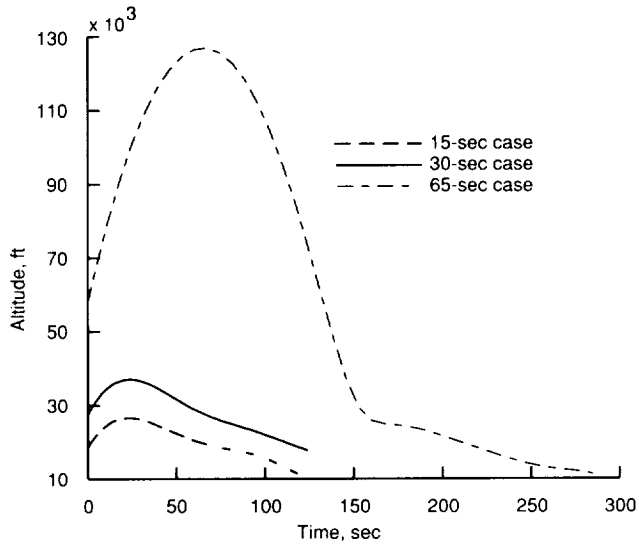

Figure 18. Altitude versus time for 15-, 30-, and 65-sec aborts.

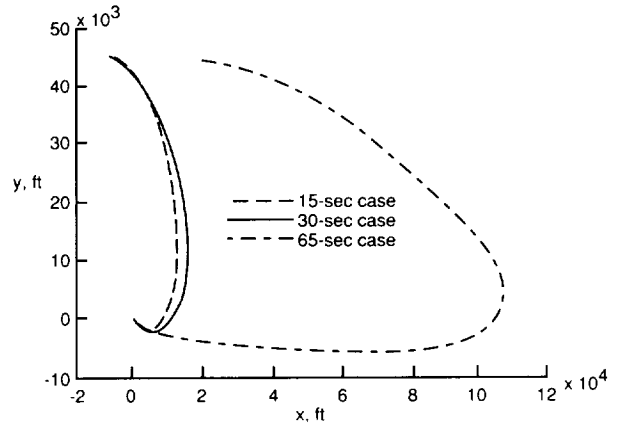

Figure 19. Ground track for 15-, 30-, and 65-sec aborts.

to 30 to 65 sec, and also shows that the 65-sec case has a much longer ground track than the other two cases (fig. 19), as would be expected from the much longer time of flight. All cases end up at the origin of the coordinate system heading in a northwesterly direction as desired.

The velocity and Mach number profiles in figures 20 and 21 show that initial velocity and Mach number increase as the launch time increases from 15 to 30 to 65 sec. They also show that for each case the velocity initially decreases as the vehicle climbs, and that after it reaches its maximum altitude the vehicle picks up speed as it dives. In the 65-sec abort case, the vehicle starts supersonic, becomes subsonic during its climb, then becomes supersonic again during the dive, and finally ends at a subsonic velocity. The final velocity in each case is the desired $V(t_f) = 520.8$ ft/sec.

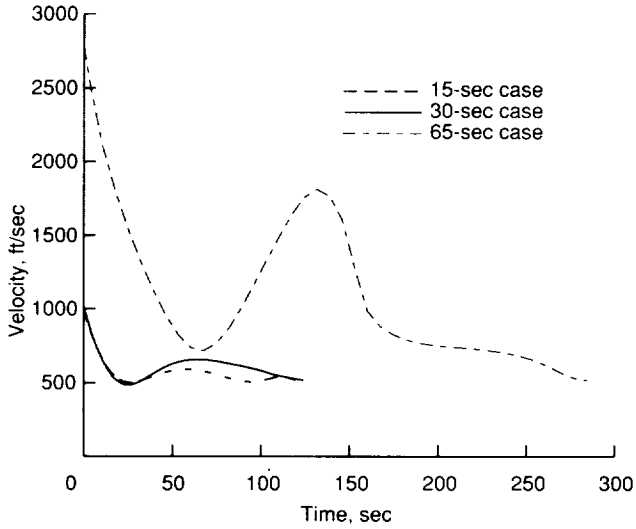

Figure 20. Velocity versus time for 15-, 30-, and 65-sec aborts.

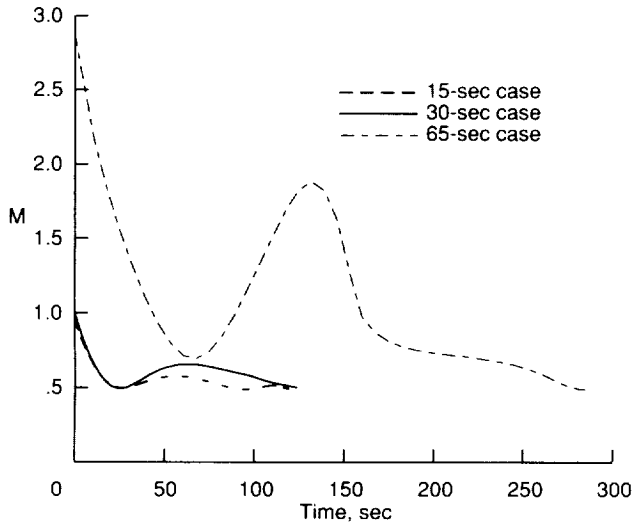

Figure 21. Mach number versus time for 15-, 30-, and 65-sec aborts.

The characteristics of climbing and losing speed and diving and gaining speed can also be seen in the flight path angle histories (fig. 22), which also show that the ascent trajectory is flattening out (decreasing $\gamma(t_0)$) as the ELV climbs from 30 to 65 sec. Oscillations are apparent in the flight path angle history, and in the 65-sec case the vehicle reaches a maximum negative γ of nearly $-80°$. The final flight path angle in each case is the desired $\gamma(t_f) = -19°$.

The heading history for each case shows nearly easterly flight along the ascent trajectory and a final heading aligned with the runway. It is also seen that in each case the vehicle wants to turn to the right (decreasing ψ) for the entire duration of the trajectory,

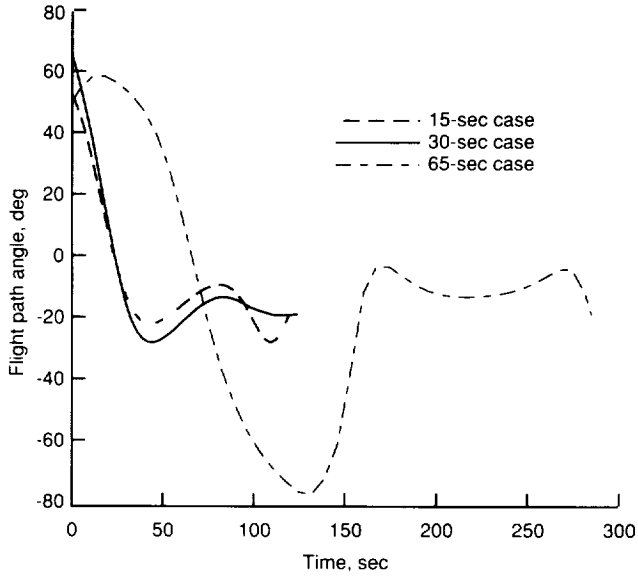

Figure 22. Flight path angle versus time for 15-, 30-, and 65-sec aborts.

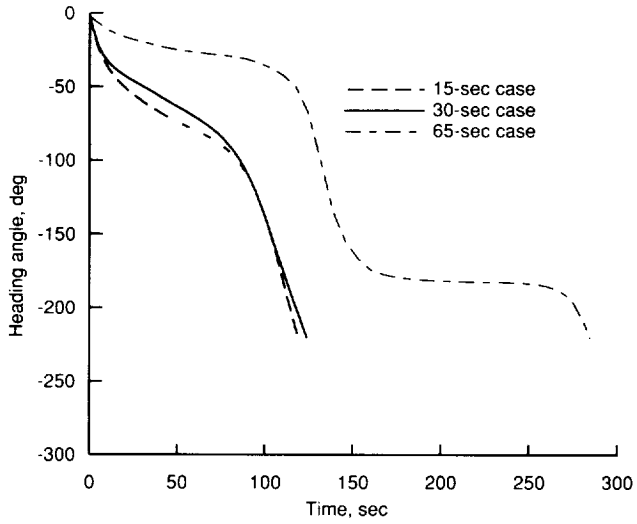

Figure 23. Heading angle versus time for 15-, 30-, and 65-sec aborts.

ending in each case at the desired $\psi(t_f) = -220.7°$ (fig. 23).

If the vehicle energy per unit mass, or specific energy, is defined as

$$E = \frac{V^2}{2} + g(h)h \tag{4.1}$$

the energy profiles (fig. 24) show that initial energy increases along the ascent trajectory and that final energy, with final velocity fixed, exhibits the same characteristic as final altitude for the three cases.

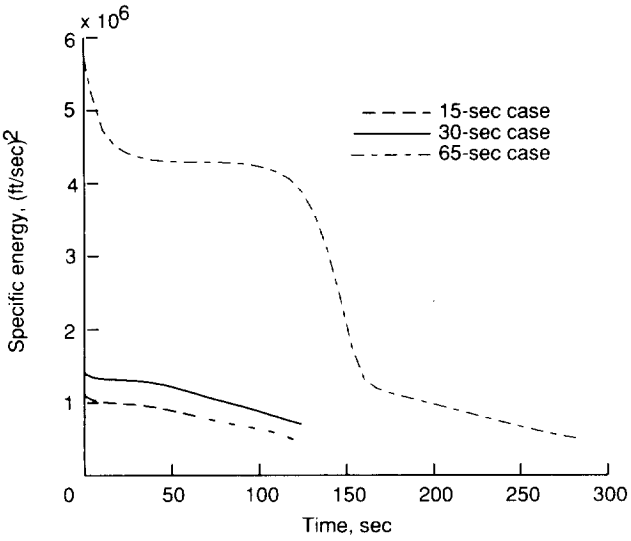

Figure 24. Energy versus time for 15-, 30-, and 65-sec aborts.

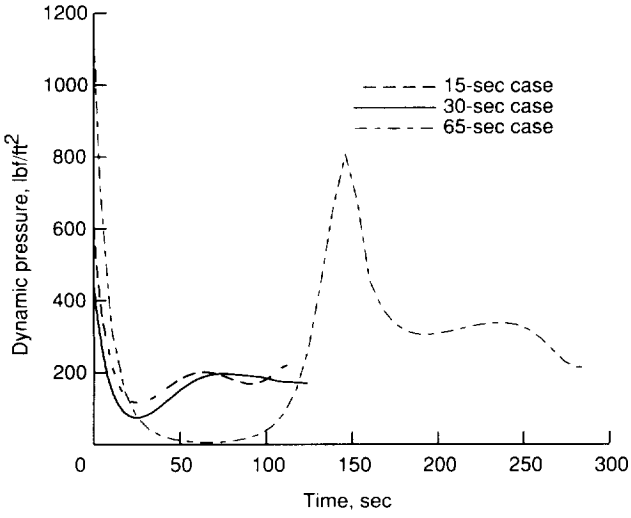

Figure 25. Dynamic pressure versus time for 15-, 30-, and 65-sec aborts.

That is, just as $h(t_f)$ for the 30-sec abort case is greater than $h(t_f)$ for the 65-sec case, which is greater than $h(t_f)$ for the 15-sec case, so is $E(t_f)$ for the 30-sec case greater than $E(t_f)$ for the 65-sec case, which is greater than $E(t_f)$ for the 15-sec case.

Dynamic pressure histories for the three cases are shown in figure 25. The maximum dynamic pressure $\bar{q}_{\max}$ occurs in each case at the initial time when the velocity is greatest. The vehicle dynamic pressure decreases immediately as the vehicle gains altitude and loses speed. When the vehicle reaches its maximum altitude and has lost a large portion of its initial speed, the dynamic pressure decreases to a point where the aerodynamic control surfaces may no longer be effective. To maintain control surface authority in this region, it may be necessary to impose a minimum dynamic pressure constraint. This becomes more important when the maximum altitude achieved for each abort case becomes increasingly greater and dynamic pressure becomes correspondingly smaller.

The normal and axial load factors, a_N and a_x, are defined for small α as

$$a_N = L/W \tag{4.2}$$

$$a_x = D/W \tag{4.3}$$

and shown in figures 26 and 27. The load factors do not present a problem in the 15- and 30-sec abort cases. During the 65-sec case however, on the pullout from the $\gamma = -80°$ dive, the load factors increase to 4.2 and 2.5 for the normal and axial directions, respectively. A constraint on the load factors can be imposed should these values be considered too large.

The reason for the high load factors can be seen from a plot of the required lift coefficient (fig. 28) calculated from the states and state rates (eq. (3.41)). For the 65-sec abort case, a spike in the C_L history occurs at the pullout of the dive, resulting directly in the normal load factor spike and, indirectly through drag coefficient, resulting in the axial load factor spike.

Figure 29 shows bank angle histories for the three cases. It is seen that for the 15- and 30-sec cases inverted flight is desired ($\sigma < -90°$) at the beginning of the trajectory, with the remainder of the trajectory flying upright. For the 65-sec case however, the vehicle begins upright, flies inverted for a time, and then ends upright with a significant portion of time spent flying with a bank angle of nearly 0°.

The vehicle could fly the initial portion of the 15- and 30-sec trajectories inverted with positive lift or upright with negative lift. It is assumed that when the lift vector is directed downward, the vehicle will fly inverted. Since there is a linear term in the C_D expression, the value of C_D for values of C_L with equal magnitude but opposite sign will not be equal. In fact, since $C_{D,1}$ is negative at most Mach numbers (except for $M = 1.6$, 2.0, and 2.5—see table III), then C_D for a positive value of C_L is less than C_D for a negative value of C_L with equal magnitude. Flying inverted with positive lift will result in lower drag than flying upright with negative lift of the same magnitude.

As stated previously, some altitude margin exists for the 15- and 65-sec abort cases. Since data were

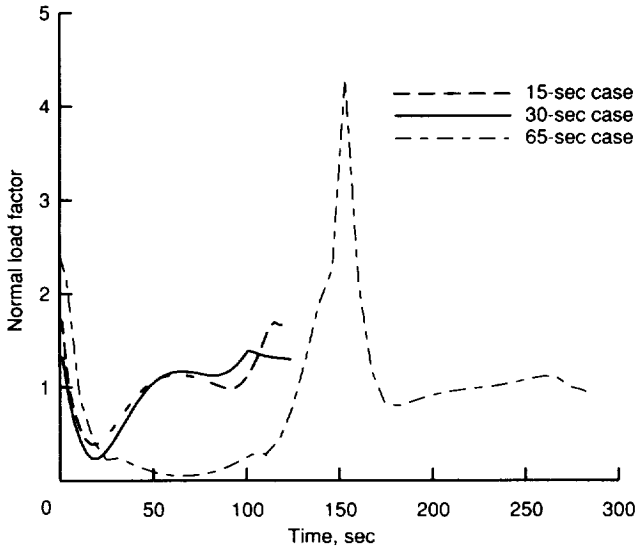

Figure 26. Normal load factor versus time for 15-, 30-, and 65-sec aborts.

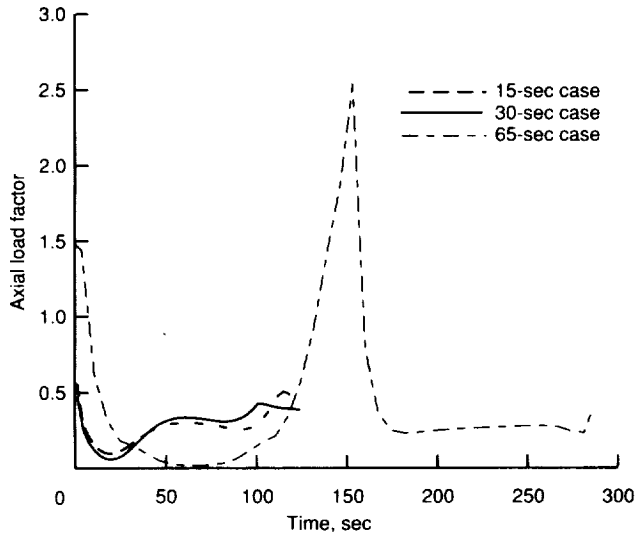

Figure 27. Axial load factor versus time for 15-, 30-, and 65-sec aborts.

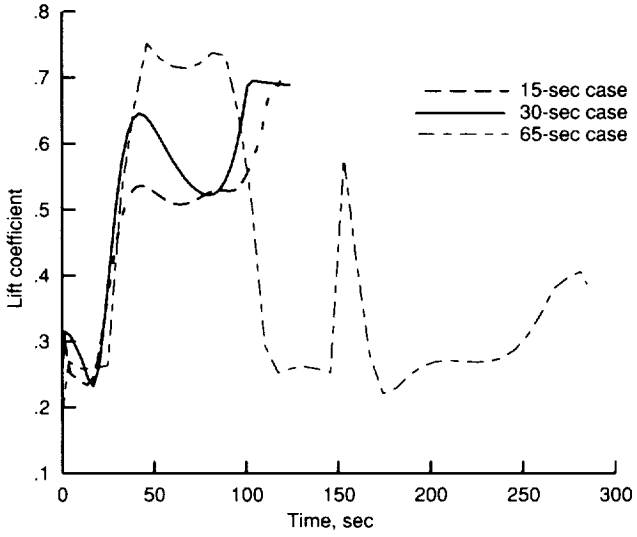

Figure 28. Lift coefficient versus time for 15-, 30-, and 65-sec aborts.

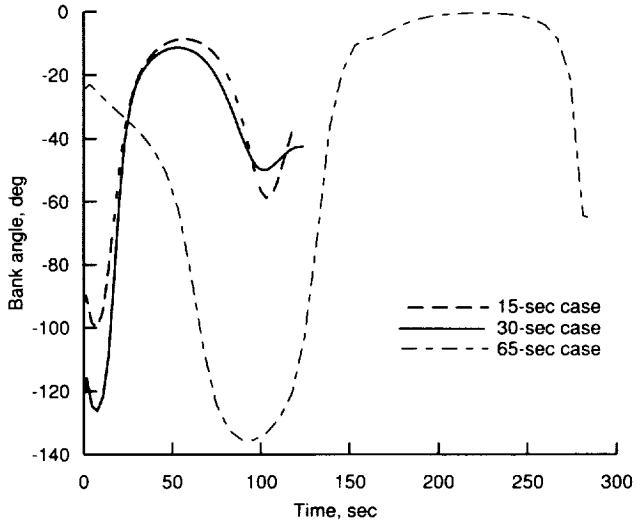

Figure 29. Bank angle versus time for 15-, 30-, and 65-sec aborts.

not available for the time before 15 sec, it is not known if an abort of this type is possible. However, applying the work in reference 11, which involved RTLS aborts to the skid strip runway 13 from the launch pad (i.e., abort time of 0 sec), the assumption can be made that RTLS aborts to the skid strip are possible at any time before 15 sec. The latest time an abort is possible would be slightly after 65 sec (but before 70 sec, since an abort was not possible at this point because of the distance of the vehicle from the skid strip). At all the times for which initial conditions are given in the tables, RTLS aborts were also possible, but the data are not shown here, since the 15-, 30-, and 65-sec cases are considered representative of all the cases.

5. Concluding Remarks

This work has applied optimal control theory to the problem of determining the feasibility of an return-to-launch-site (RTLS) abort of an HL-20 vehicle carried into orbit by a Titan III expendable launch vehicle (ELV). The trajectories that resulted, in which final altitude near the runway was maximized, were not the trajectories the HL-20 would follow to return to the skid strip at Cape Canaveral Air

Force Station. Although the problem of determining the actual RTLS abort trajectory is also of interest for the trajectory planner, that was not covered here.

It was found that for an HL-20 launched from Kennedy Space Center (KSC) pad 40, RTLS aborts could be performed to runway 31 of the KSC skid strip between the launch times of 15 sec and 65 sec, after which, though the vehicle energy has increased, the vehicle is too far away to glide back.

Maximizing final altitude with final velocity fixed is nearly the same problem as maximizing final energy (or minimizing energy loss). The minimum energy loss problem has application in the calculation of the maximum achievable ground coverage, or footprint, of a reentry vehicle or the abort paths of vehicles such as the National Aero-Space Plane.

Additional future work in the area of optimal RTLS aborts could involve shaping the ascent trajectory of an ELV to maximize the amount of time during which an RTLS abort could be performed. The use of the orbital maneuvering system engines during the abort phase and adding guidance logic to the primary and sustainer solid rocket motor burns could also be investigated.

NASA Langley Research Center
Hampton, VA 23681-0001
April 21, 1994

6. References

1. Talay, Theodore A.; and Stone, Howard W.: The Personnel Launch System—A Lifting Body Approach. IAF Paper 91-202, Oct. 1991.

2. Naftel, J. Chris; Powell, Richard W.; and Talay, Theodore A.: Performance Assessment of a Space Station Rescue and Personnel/Logistics Vehicle. *J. Spacecr. & Rockets*, vol. 27, no. 1, Jan.–Feb. 1990, pp. 76–81.

3. Naftel, J. C.; and Talay, T. A.: Ascent Abort Capability for the HL-20. *J. Spacecr. & Rockets*, vol. 30, no. 5, Sept.–Oct. 1993, pp. 628–635.

4. Chern, Jeng-Shing; and Vinh, Nguyen Xuan: *Optimum Reentry Trajectories of a Lifting Vehicle.* NASA CR-3236, 1980.

5. Bryson, Arthur E., Jr.; and Ho, Yu-Chi: *Applied Optimal Control*, Revised printing. Hemisphere Publ. Corp., 1975.

6. Jackson, E. Bruce; Cruz, Christopher I.; Ragsdale, W. A.: *Real-Time Simulation Model of the HL-20 Lifting Body.* NASA TM-107580, 1992.

7. Gill, Philip E.; Murray, Walter; Saunders, Michael A.; and Wright, Margaret H.: *User's Guide for NPSOL (Version 4.0): A Fortran Package for Nonlinear Programming.* Tech. Rep. SOL 86-2, Stanford Univ., Jan. 1986.

8. *U.S. Standard Atmosphere, 1962.* NASA, U.S. Air Force, and U.S. Weather Bureau, Dec. 1962.

9. Seywald, Hans: *Trajectory Optimization Based on Differential Inclusion.* NASA CR-4501, 1993.

10. Cliff, Eugene M.; Seywald, Hans; and Bless, Robert R.: Hodograph Analysis in Aircraft Trajectory Optimization. AIAA Guidance, Navigation, and Control Conference. Tech. Papers Pt. 1, AIAA, 1993, pp. 363–371. (Available as AIAA-93-3742.)

11. Jackson, E. Bruce; Rivers, Robert A.; Chowdhry, Rajiv S.; Ragsdale, W. A.; and Geyer, David W.: Investigation of the Launch Pad Abort Capabilities of the HL-20 Lifting Body. AIAA-93-3690, Aug. 1993.

REPORT DOCUMENTATION PAGE

Form Approved
OMB No. 0704-0188

1. AGENCY USE ONLY *(Leave blank)*	2. REPORT DATE	3. REPORT TYPE AND DATES COVERED
	July 1994	Technical Paper

4. TITLE AND SUBTITLE
Optimal Control Theory Determination of Feasible Return-to-Launch-Site Aborts for the HL-20 Personnel Launch System Vehicle

5. FUNDING NUMBERS
WU 506-59-61-04

6. AUTHOR(S)
Kevin E. Dutton

7. PERFORMING ORGANIZATION NAME(S) AND ADDRESS(ES)
NASA Langley Research Center
Hampton, VA 23681-0001

8. PERFORMING ORGANIZATION REPORT NUMBER
L-17343

9. SPONSORING/MONITORING AGENCY NAME(S) AND ADDRESS(ES)
National Aeronautics and Space Administration
Washington, DC 20546-0001

10. SPONSORING/MONITORING AGENCY REPORT NUMBER
NASA TP-3449

11. SUPPLEMENTARY NOTES

12a. DISTRIBUTION/AVAILABILITY STATEMENT
Unclassified - Unlimited

Subject Category 18

12b. DISTRIBUTION CODE

13. ABSTRACT *(Maximum 200 words)*

The Personnel Launch System (PLS) being studied by NASA is a system to complement the Space Shuttle and provide alternative access to space. The PLS consists of a manned spacecraft launched by an expendable launch vehicle (ELV). A candidate for the manned spacecraft is the HL-20 lifting body. In the event of an ELV malfunction during the initial portion of the ascent trajectory, the HL-20 will separate from the rocket and perform an unpowered return-to-launch-site (RTLS) abort. This work details an investigation, using optimal control theory, of the RTLS abort scenario. The objective of the optimization was to maximize final altitude. With final altitude as the cost function, the feasibility of an RTLS abort at different times during the ascent was determined. The method of differential inclusions was used to determine the optimal state trajectories, and the optimal controls were then calculated from the optimal states and state rates.

14. SUBJECT TERMS
Return-to-launch-site aborts; HL-20; Optimal control theory; Personnel Launch System

15. NUMBER OF PAGES
24

16. PRICE CODE
A03

17. SECURITY CLASSIFICATION OF REPORT	18. SECURITY CLASSIFICATION OF THIS PAGE	19. SECURITY CLASSIFICATION OF ABSTRACT	20. LIMITATION OF ABSTRACT
Unclassified	Unclassified		

NSN 7540-01-280-5500

Standard Form 298(Rev. 2-89)
Prescribed by ANSI Std. Z39-18
298-102